Geomorphology 116 (2010) 189–201

Contents lists available at ScienceDirect

Geomorphology

journal homepage: www.elsevier.com/locate/geomorph

Controls of glacial valley spacing on earth and mars

Jon D. Pelletier [a,*], Darin Comeau [b], Jeff Kargel [c]

[a] Department of Geosciences, University of Arizona, 1040 East Fourth Street, Tucson, AZ 85721, USA
[b] Department of Applied Mathematics, University of Arizona, Tucson, AZ 85721, USA
[c] Department of Hydrology and Water Resources, University of Arizona, Tucson, AZ 85721, USA

ARTICLE INFO

Article history:
Received 16 June 2009
Received in revised form 20 October 2009
Accepted 24 October 2009
Available online 1 November 2009

Keywords:
Glacial erosion
Numerical modeling
Rocky mountains
Mars

ABSTRACT

Low-order alpine glacial valleys on Earth commonly have a characteristic spacing of 1–3 km. Here we develop analytic and numerical solutions of a coupled numerical model for alpine glacial flow and subglacial bedrock erosion to quantitatively determine the controls on glacial valley spacing assuming an initially-undissected landscape, an initially-fluvially-dissected landscape, and an initially-cratered landscape. The characteristic spacing of glacial valleys produced by the model is controlled by a competition between the thickening of ice in incipient glacial valleys, which acts to enhance flow and valley deepening, and viscous/sidewall drag, which acts to limit flow and deepening. The glacial valley spacing that represents the best compromise between these two competing effects is found to be a function of valley slope, the threshold basal shear stress for ice motion, the effective ice viscosity, a bed-friction parameter, and gravity. This model framework provides the preliminary basis for understanding the relative spacing of glacial valleys on Earth and Mars. On Mars, montane glacial valleys have widths and spacings that are approximately 10–20 times larger than those on Earth. Model results suggest that this difference is predominantly a consequence of lower bed slopes and larger temperature-controlled ice viscosities of glacial ice on Mars compared to Earth.

1. Introduction

Fluvial valleys that form in the absence of structural control are characteristically V-shaped while glacial valleys are characteristically U-shaped. Numerical modeling has been successful in reproducing the transition between these two characteristic forms. Starting from a V-shaped valley with a prescribed width and height, Harbor (1992a,b,c) quantified the transition to a U-shaped valley through time following the introduction of an alpine glacier into the valley. A number of studies (e.g., Harbor, 1992c; Seddik et al., 2005) have explored the specific functional form of glacial valleys, e.g. is the valley cross-sectional profile best fit by a parabola or a catenary? Most of these studies are limited to 2D, however, and hence may not capture important 3D effects of converging and diverging ice flow in glacial valleys. Also, just as important as the functional form of the valley cross section is the fact that low-order glacial valleys tend to be quasi-periodic with a characteristic spacing of approximately 1–3 km. What controls this fundamental length scale of low-order glacial valleys? Fluvial valleys, in contrast, vary in width and spacing over a much wider range of scales, i.e. from tens of meters to several kilometers, depending on drainage basin size, bedrock erodibility, uplift rate and other factors. In this paper, we investigate the relationship between ice flow and subglacial bedrock erosion in alpine glacial environments in order to determine the factors that control the spacing of low-order glacial valleys.

Recent modeling work on the coupled evolution of glacial flow and erosion has illuminated the feedbacks between glacial erosion, climate change, and tectonics (e.g. Herman and Braun, 2008). No study has yet provided a better fundamental understanding of the controls on glacial valley spacing using a 3D model, however, in part because sidewall drag is included in most numerical models in only an approximate way. In Herman and Braun (2008), for example, sidewall drag is included in the model by reducing the basal flow velocities by an amount related to the product of a prescribed "constriction factor" (which has units of length) and the cross-sectional valley curvature (units of one over length). The glacial valley width and spacing that result from models that use a constriction-factor-based approach to quantifying sidewall drag depend directly on the value of this constriction factor. As such, the glacial valley spacing is an input rather than an output in such models. Fundamentally, the constriction factor must depend on the flow rheology (e.g. viscosity) and frictional parameters of the bed. In order to better understand the controls on glacial valley morphology and spacing, a more comprehensive approach is needed that quantifies the sidewall drag of alpine glaciers as a function of the fundamental parameters that define the rheology of the flow and the friction parameters of the bed (Table 1).

To put the characteristic size of glacial valleys into perspective, it is useful to compare glacial valleys on Earth with those on Mars. In the regions of the Argyre and Hellas Basins of the southern hemisphere of Mars, crater walls have been sculpted into cirque-like basins (Kargel

* Corresponding author. Tel.: +1 520 331 2576; fax: +1 520 621 2672.
E-mail address: jdpellet@email.arizona.edu (J.D. Pelletier).

0169-555X/$ – see front matter © 2009 Elsevier B.V. All rights reserved.
doi:10.1016/j.geomorph.2009.10.018

Table 1
Definitions of model variables and parameters.

Variable/ parameter	Description	Representative value/range used here (if applicable)
a	Coefficient in Hallet erosion model	
A	Coefficient in Glen's flow law	5×10^{-15} (kPa)$^{-3}$ s^{-1} for $T=0$ °C, but varies with T
A_d	Drainage area (fluvial model)	
b	Exponent in Hallet erosion model	1
c	Bed-friction parameter	3×10^{-17}–3×10^{-15} Pa^{-2} m s^{-1}
E	Spatially-averaged erosion rate	
ε	Amplitude of bed perturbation	
g	Acceleration due to gravity	9.81 m s^{-2} (Earth), 3.72 m s^{-2} (Mars)
$h(x,y)$	Ice thickness	
h_0	Average ice thickness	
h_1	Ratio of amplitude of ice thickness perturbations to bed topography variations	
K	Bedrock erodibility coefficient (fluvial model)	
λ	Wavelength of bed perturbation	
λ_{max}	Fastest-growing wavelength	
$M(x,y)$	Ice mass balance (3D model)	
m_1	Mass balance gradient above ELA (3D)	0.01 yr^{-1}
m_2	Mass balance gradient below ELA (3D)	0.03 yr^{-1}
μ	Ice viscosity	10^{14} Pa s, but varies with T
ρ	Ice density	920 kg m^{-3}
$q(x,y)$	Ice flux (3D model)	
S	Ice surface slope in radians	
T	Time	
T	Ice temperature in degrees Celsius	
Θ	Bed surface slope in radians	
τ_b	Basal shear stress	
τ_y	Threshold shear stress for motion	0.1–1.0 bars
τ_γ	τ_y divided by ρg	
u_s	Basal sliding velocity	
u_{s1}	Amplitude of perturbations in u_s	
$u(x,y)$	Depth-averaged ice velocity (3D model)	
U	Rock uplift rate (fluvial model)	
X	Distance along valley cross section	
X	$2\pi x/\lambda$	
Y	Distance down valley	
$z(x,y)$	Bedrock elevation	
z_{ELA}	Equilibrium line altitude (3D model)	

and Strom, 1992). These landforms have been used, as one component of an assemblage of landforms morphologically similar to glacial landforms on Earth, to argue for warm-based glaciation on Mars (Kargel and Strom, 1992). These cirque-like landform grade downslope into sinuous ridges that share many similarities with terrestrial eskers (Banks et al., 2009). Erosional grooves and streamlined hills are also present in the high resolution imagery of these regions (Banks et al., 2009). The characteristic size of cirque-like landforms in the Argyre region of Mars is approximately 10–20 times larger than those on Earth (Kargel, 2004). The reason for this difference is unclear, but possible reasons include differences in gravity, ice thickness, valley slope, ice viscosity, and bed-friction parameters between the two planets. Differences in viscosity and bed friction may ultimately be related to differences in temperature within the ice.

In this paper, we investigate the controls on glacial valley spacing, motivated by the question of what factors lead to the order-of-magntiude difference in the characteristic scales of low-order glacial valleys on Earth and Mars. We begin by quantifying the characteristic spacing of glacial valley cross-sectional profiles on Earth and Mars using Digital Elevation Model (DEM) analysis. We then develop a mathematical model for the flow of ice over complex topography and the glacial erosion that results from that flow. The model is first analyzed using a linear stability analysis that poses the question: given an initially-undissected sloping terrain with small-amplitude variations in bed topography (i.e. incipient glacial valleys), which glacial valleys grow the most rapidly? The fastest-growing incipient valleys predicted by this analysis represent a compromise between the thickening of ice in incipient glacial valleys, which increases flow and erosion, and viscous stresses/sidewall drag, which act to limit flow and erosion. Conceptually, the model suggests that very narrow, deeply-incised glacial valleys do not form (or form very slowly) because increased bed friction and viscous stresses within such narrow valleys limit basal sliding and erosion. This limiting effect favors the formation of relatively wide valleys in the competition between incipient valleys with a range of spacings as an initially-undissected landscape begins to be incised. Linear stability analyses are only precisely applicable when incipient valleys are small in amplitude. Nonetheless, linear stability analyses are often useful in quantitatively determining how the spacing of a given instability is controlled by the fundamental parameters of the model. The results of the linear stability analysis in this paper reveal that the spacing of glacial valleys that grow most rapidly (and hence are favored to form well-developed glacial valleys) is a function of valley slope, the threshold basal shear stress for ice motion, ice viscosity, a bed-friction parameter that controls how rapidly the glacier slides along its base for a given basal shear stress, and gravity. The importance of these controlling factors is confirmed by 3D numerical models that track the formation of well-developed glacial valleys from initially-undissected topography, initially-fluvially-dissected topography, and initially-cratered topography. The characteristic size of glacial valleys produced by the model is not very sensitive to whether the topography is initially undissected, initially-fluvially dissected, or initially cratered. The version of the model with initially-fluvial topography, for example, exploits preexisting fluvial valleys but the characteristic spacing of those valleys increases over time to match those of the case with initially-undissected topography. Given sufficient time, therefore, a fluvial landscape can be completely "reset" above the equilibrium line by glacial erosion.

2. DEM analysis and observations

The purpose of this section is to place quantitative constraints on the spacing of low-order glacial valleys on Earth and Mars. Fig. 1 illustrates examples of terrestrial alpine glacial topography from the Absaroka, Uinta, and central Rocky Mountains of the United States. The highest elevations in each of these ranges are dominated by low-order cirque basins with characteristic spacings of 1–3 km. Fig. 2A–C plots selected topographic cross sections from the low-order valleys of each range, illustrating the periodic nature of the topography and the U-shaped character of the valleys. Cirque valleys at the highest elevations are tributaries to larger glacial valleys with spacings of 5–10 km. Our focus in this paper is on the characteristic spacing of the low-order glacial valleys. The spacing of higher-order valleys is more difficult to interpret uniquely in terms of ice rheology and the processes of glacial erosion because those valleys may be inherited from the fluvial system and/or may be controlled by the large-scale structural and tectonic history of each mountain range. The spacing of low-order glacial valleys in these ranges is remarkably consistent despite differences in rock type, structure, etc. between each range.

Evidence for warm-based glaciation in the vicinity of the Argyre and Hellas basins of Mars (Fig. 3) has been steadily accumulating in recent years. Kargel and Strom (1992) first proposed the glacial erosion hypothesis for these regions based on the morphological similarity between erosionally-modified craters with cirque basins and U-shaped valleys on Earth. The fact that water or CO_2 ice could flow under Martian conditions has long been established (e.g. Clark and Mullin, 1976). The regions of Argyre and Hellas Basins are home to glacial ice today in the form of lobate debris aprons. Holt et al. (2008) and Plaut et al. (2009) recently documented that some of these landforms are rock-covered glaciers that under present conditions are

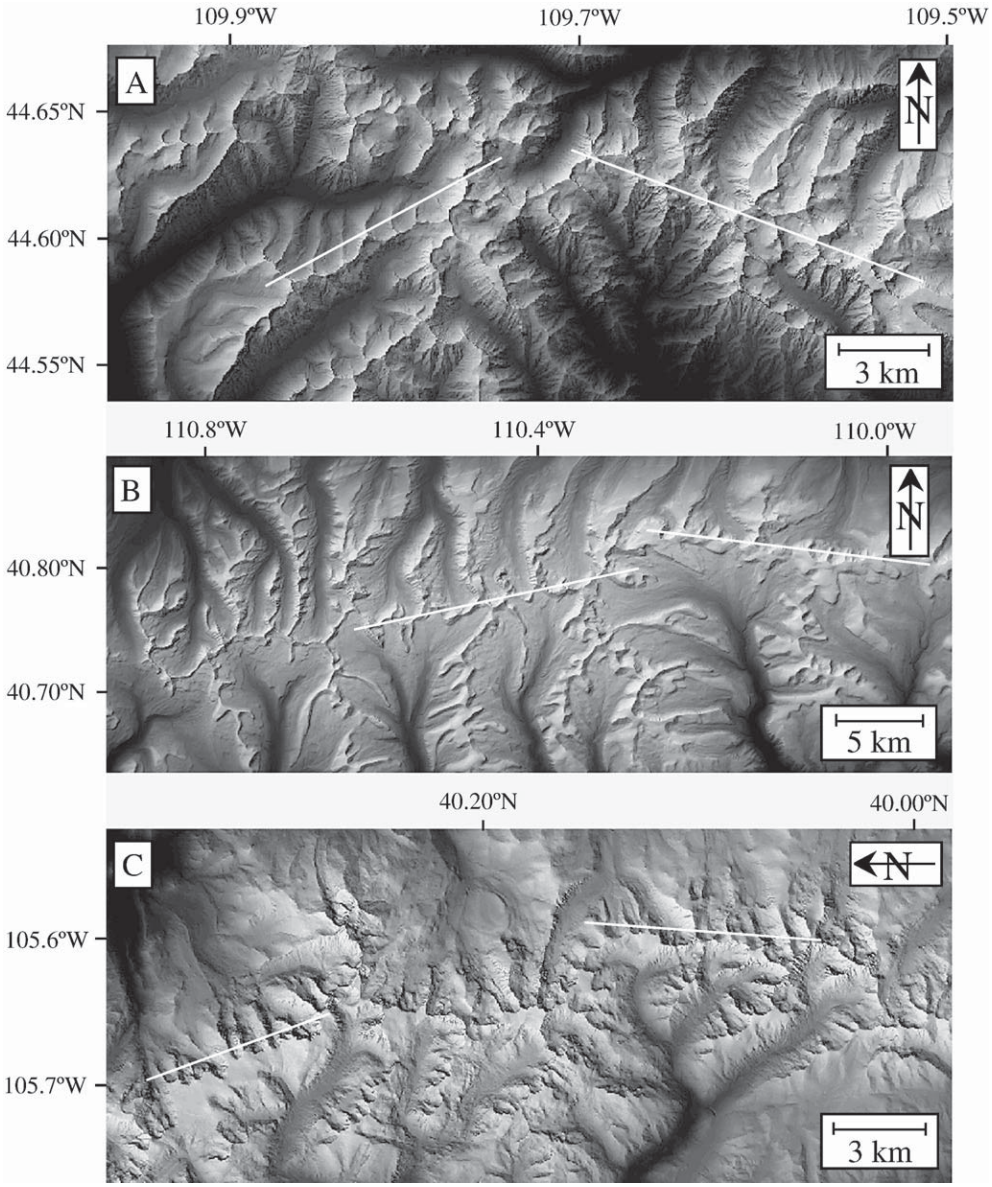

Fig. 1. Shaded-relief images of glacially-eroded topography in the United States using U.S. Geological Survey 30 m/pixel DEMs. (A) Beartooth-Absaroka Mountains, Montana, (B) Uinta Mountains, Utah, and (C), central Rocky Mountains, Colorado. The locations of topographic profiles plotted in Fig. 2 are shown as white lines.

likely cold-based (and hence have limited erosive power) but may have expanded and eroded the adjacent highlands under conditions of higher obliquity. Numerous wide crater breaches suggest that warm-based glaciers filling craters eroded crater walls as ice spilled over the edges. In addition, Banks et al. (2009) recently analyzed a suite of depositional landforms in the lower elevations of Argyre Basin using (High Resolution Imaging Science Experiment) HiRISE imagery, including sinuous ridges and longitudinal grooves. Many of these landforms on Mars share striking similarities with terrestrial eskers and glacially-carved grooves on Earth.

The characteristic scale of glacial landforms on Mars is much larger than those on Earth. Fig. 2D illustrates that "cirque" valleys on Mars occur with characteristic spacings of 10–30 km. Glaciation on Mars is also different from that on Earth due to the nature of the preexisting topography. Meteors continuously bombard the Martian surface and create impact basins with a wide range of sizes. Glacial modification of crater rims creates embayments of the larger craters that ring the Argyre and Hellas basins at a scale set by the coupled behavior of ice flow and subglacial bedrock erosion. What determines that scale on both Earth and Mars is the central question of this paper. The strength of gravity and the threshold basal stress of ice on Mars will both be different from those on Earth, of course. Differences in gravity and threshold basal shear stress may not play a dominant role in influencing the relative scale of glacial erosion on the two planets, however, because these two effects partly offset one another. Threshold basal shear stress and gravity both control ice thickness, a variable that certainly plays a role in controlling glacial valley spacing. However, it is the *ratio* of the threshold basal shear stress to gravity that controls the thickness of ice, and the threshold basal shear stress on Mars is lower than that on Earth, as is gravity. Inferred threshold basal shear stresses in the south polar ice cap of Mars are about half that of modern terrestrial ice sheets (Banks and Pelletier, 2008). For the same bed topography, this implies that ice thicknesses on Mars are comparable to those on Earth because the lower gravity on Mars (about 40% that of Earth) offsets the lower threshold basal shear stresses to a significant extent. This suggests that the primary cause

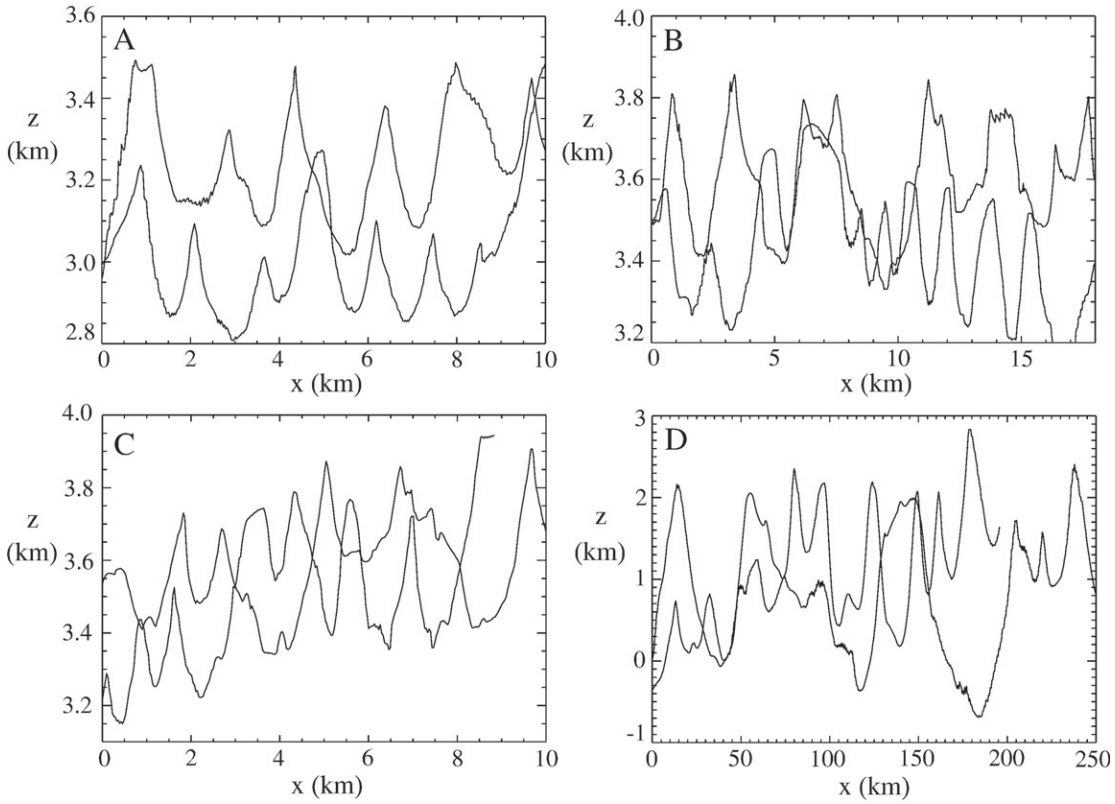

Fig. 2. Plots of topographic cross-sectional profiles extracted from the DEMs of Earth and Mars. (A) Beartooth-Absaroka Mountains, Montana, (B) Uinta Mountains, Utah, (C) central Rocky Mountains, Colorado and (D) Argyre Basin, Mars. See Figs. 1 and 3 for profile locations.

for the vastly different scales of glacially-eroded landforms on Earth and Mars is not simply the result of the difference in gravity.

Typical bed slopes within formerly glaciated areas of Mars are several times smaller than those of typical alpine glacial valleys on Earth. Slopes in glacial valleys are highly variable, but average slopes at the scale of glacial valleys can be estimated using the relief ratio, defined as the ratio of the relief to the lateral distance over which that relief is calculated. In the terrestrial areas illustrated in Fig. 1, relief is approximately 0.5 km over spatial scales of 1–3 km, yielding relief ratios in the range of 0.15–0.5. On Mars, relief is greater, increasing up to 2 km, but distances along and between valleys increases by an even greater amount, from 1–3 km to a typical range of 10–30 km. As such, relief ratios of formerly glaciated highland regions on Mars are in the range of 0.05–0.1, or approximately 2–6 times smaller than those on Earth. Bed slopes control the thickness of ice for a given yield stress (with steeper slopes resulting in thinner ice), hence if ice thickness controls glacial valley spacing it is likely that differences in bed slope between the two planets will play a significant role on controlling differences in glacial valley spacing.

3. Model description and results

3.1. Description

For a given lithology, the rate of glacial erosion can be controlled by basal sliding velocity, ice thickness, or a combination of the two. Boulton (1974) emphasized the role of ice thickness in determining erosion rates, while Hallet (1979) emphasized the importance of sliding velocity. In Boulton's model, the hydrostatic pressure induced by the ice overburden pressure increases the normal stress acting on subglacial debris, which, in turn increases its ability to abrade the bed. In Hallet's model, ice thickness is not a factor because hydrostatic pressures are assumed to act equally on the tops and bottoms of rounded subglacial particles. In Hallet's model, the velocity of the abrading particles, embedded in the ice, is the most important controlling factor for erosion. Hallet's model can be summarized as

$$\frac{\partial z}{\partial t} = -a|u_s|^b \tag{1}$$

where $\partial z/\partial t$ is the erosion rate, $|u_s|$ is the basal sliding speed, and a and b are empirical coefficients. The value of b is assumed to be 1 in some studies (Harbor, 1992a,b; Tomkin and Braun, 2002; Herman and Braun, 2008) and 2 in others (MacGregor et al., 2000, 2009). A value of b greater than 1 is consistent with the conceptual model that more erosion provides the "cutting tools" that lead to enhanced bedrock erosion downvalley. The value of a may be constrained for a given area using sediment-flux estimates from modern glaciers (e.g. Hallet et al., 1996).

Theoretical models suggest that basal sliding velocity depends on the square of the basal shear stress (Weertman, 1957):

$$u_s = DR^{-4}\tau_b^2 = c\tau_b^2 \tag{2}$$

where D is a constant primarily dependent on the thermal properties of the ice and rock, R is the ratio of the characteristic size of obstacles to their spacing on the bed, and τ_b is the basal shear stress. Here we combine D and R into a single parameter c equal to the product DR^{-4}. We refer to c as the bed-friction parameter because it controls the rate of sliding for a given basal shear stress. The value of c can be approximately constrained by noting that, in low-order terrestrial alpine glaciers, basal shear stresses are on the order of 0.1–1 bar (10^4–10^5 Pa) and sliding velocities are on the order of 1–10 m yr^{-1}. These values constrain c to be approximately in the range of 3×10^{-17} to 3×10^{-15} Pa^{-2} m s^{-1} for low-order terrestrial alpine glaciers.

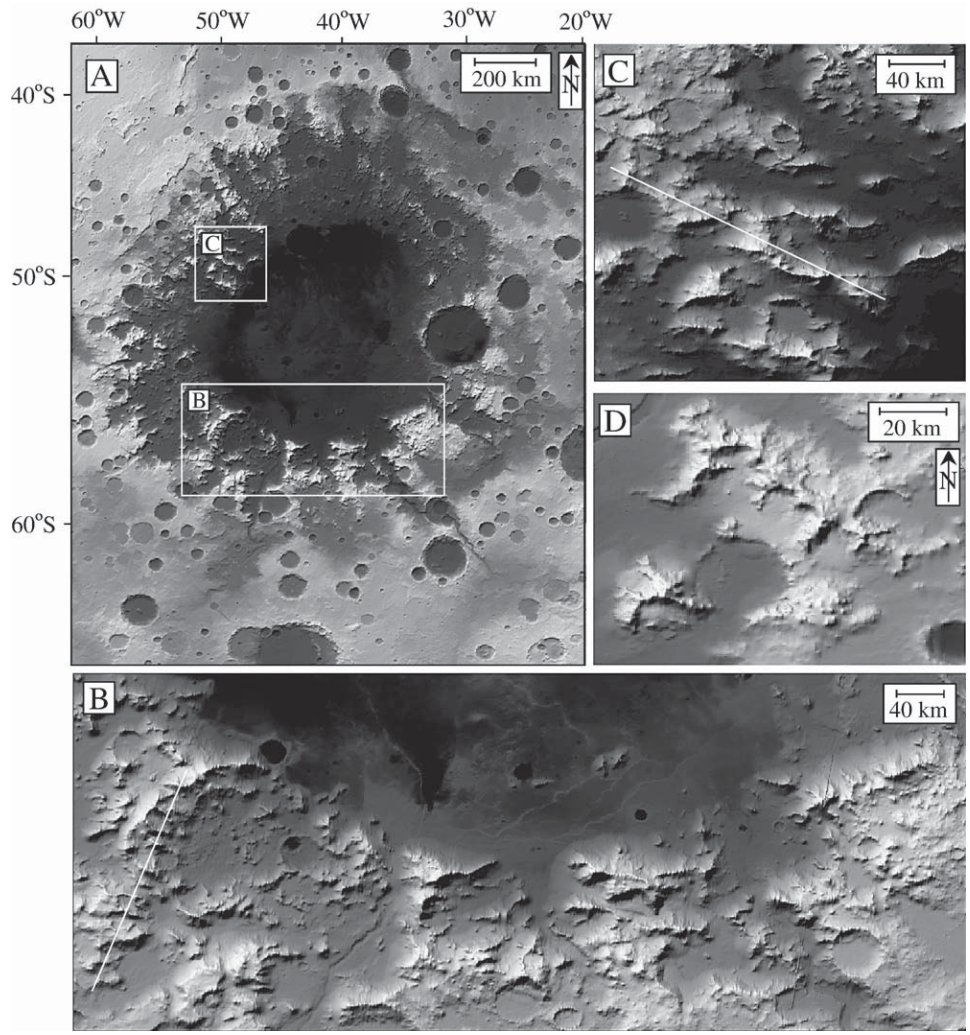

Fig. 3. Shaded-relief images of topography in the Argyre Basin, Mars, using Mars Orbital Laser Altimeter (MOLA) gridded data (Smith et al., 2003). (A) Overview map. (B and C) Closeup images. (D) Area of lobate debris aprons and possible glacially-eroded topography near Hellas Basin. The locations of topographic profiles plotted in Fig. 2 are shown as white lines.

τ_b in a wide alpine glacier is given by (Nye, 1951)

$$\tau_b = \rho g h \sin S \tag{3}$$

where ρ is the density of ice, g is the acceleration due to gravity, h is the ice thickness, and S is the ice surface slope. For a sloping bed of mean gradient $\tan\theta$ and variations in bed elevation and ice thickness given by $z(x,y)$ and $h(x,y)$, respectively, Eq. (3) can be written as

$$\tau_b = \rho g h \cos\theta \sqrt{\left(\frac{\partial z}{\partial y} + \frac{\partial h}{\partial y}\right)^2 + \left(\frac{\partial z}{\partial x} + \frac{\partial h}{\partial x}\right)^2} \tag{4}$$

Eq. (4) holds for a wide, shallow glacier in which sidewall drag can be neglected. In alpine glacial environments where sidewall drag cannot be neglected, it is necessary to modify Eq. (4) by adding an additional term that has units of shear stress. Conceptually, this term must be proportional to the cross-sectional bed curvature, $|\partial^2 z/\partial x^2|$, because the more tightly curved the cross-sectional bed topography is, the larger the sidewall drag will be. As the sliding ice flows down incipient valleys, variations in sliding velocity u_s that result from bed friction will trigger viscous stresses within the flow that are proportional to the effective ice viscosity. The effective ice viscosity μ depends on thermal and material properties of the ice and on the stress state of the ice, but for ice under shear stress and temperature conditions common in terrestrial environments the effective ice viscosity is on the order of 10^{14} Pa s (Paterson, 2000). The only term that combines $|\partial^2 z/\partial x^2|$, u_s, and μ that has the units of shear stress is the product of these three variables, i.e. $\mu|\partial^2 z/\partial x^2|u_s$. Subtracting this sidewall/viscous drag term from Eq. (4) gives

$$\tau_b = \rho g h \cos\theta \sqrt{\left(\frac{\partial z}{\partial y} + \frac{\partial h}{\partial y}\right)^2 + \left(\frac{\partial z}{\partial x} + \frac{\partial h}{\partial x}\right)^2} - \mu \left|\frac{\partial^2 z}{\partial x^2}\right| u_s \tag{5}$$

Conceptually, Eq. (5) suggests that the spacing of glacial valleys will be determined by a competition between two effects. Spatially-concentrated ice flow causes localized valley erosion in a positive feedback of localized ice thickening and erosional deepening. This effect is represented quantitatively by the h, $\partial z/\partial x$, and $\partial h/\partial x$ factors in the first term on the right side of Eq. (5). The development of narrow glacial valleys with high curvature, however, generates viscous shear stresses and sidewall drag that act to limit sliding velocities. This effect is represented by the second term on the right side of Eq. (5). Substituting Eq. (2) into Eq. (5) gives

$$\tau_b = \rho g h \cos\theta \sqrt{\left(\frac{\partial z}{\partial y} + \frac{\partial h}{\partial y}\right)^2 + \left(\frac{\partial z}{\partial x} + \frac{\partial h}{\partial x}\right)^2} - \mu c \left|\frac{\partial^2 z}{\partial x^2}\right| \tau_b^2 \tag{6}$$

i.e. a quadratic equation for τ_b. Given values for $z(x,y)$ and $h(x,y)$ for each time step, τ_b can be computed by solving Eq. (6), u_s can then be

computed using Eq. (2), and erosion rates can be computed using Eq. (1). In the model, the variables μ and c always appear as a product. Since their values are very high and low, respectively, in mks units, it is useful to give a representative value for the range of their product. A representative range of μc is approximately 0.003–0.3 m Pa^{-1} for terrestrial glaciers, given $c = 3\times10^{-17}$–3×10^{-15} Pa^{-2} m s^{-1} and $\mu \sim 10^{14}$ Pa s.

3.2. Linear stability analysis

In this section we calculate the growth rates of incipient, small-amplitude glacial valleys as a function of the wavelength of those valleys and the fundamental parameters of the model. For the purposes of this analysis, the ice thickness h is assumed to have a constant spatially-averaged value given by

$$h_0 = \frac{\tau_\gamma}{\sin\theta} \tag{7}$$

In Eq. (7), τ_γ (units of length) is equal to $\tau_y/\rho g$, where τ_y (units of Pascals) is the threshold basal shear stress for the motion of ice over bedrock. Threshold basal shear stresses of terrestrial glaciers are commonly in the range of 0.3–1 bars (1 bar equals 10^5 Pa), resulting in a range of values for τ_γ from 3 to 10 m for both terrestrial glaciers and modern ice caps on Mars (where lower gravity is accompanied by lower threshold basal shear stresses; Banks and Pelletier, 2008). Ice is thicker in incipient valleys and thinner on incipient interfluves, but the assumption of a reference spatially-averaged value h_0 simplifies the analysis so that the results can be written in terms of an average ice thickness or threshold basal shear stress rather than a mass accumulation function.

The linear stability analysis begins by assuming an initially-undissected sloping bed with a uniform gradient $\tan\theta$ and a cross-sectional sinusoidal variation in bed topography with amplitude ε given by

$$z = \tan\theta y + \varepsilon\cos\left(\frac{2\pi x}{\lambda}\right) \tag{8}$$

where λ is the wavelength of the sinusoidal variation. The ice thickness is given by the reference value in Eq. (7) minus a sinusoidal variation that mimics the variations in bed topography:

$$h = \frac{\tau_\gamma}{\sin\theta} - \varepsilon h_1\cos\left(\frac{2\pi x}{\lambda}\right) \tag{9}$$

The variable h_1 in Eq. (9) is a nondimensional factor between 0 and 1 that represents the relative amplitude of variations in ice thickness to variations in bed topography. If h_1 equals 1, the ice surface is flat and variations in h are a mirror image of variations in z. If h_1 equals 0, the ice surface is follows the bed topography and h is uniform even though the bed topography is variable.

To solve for h_1, it is necessary to introduce an additional model element that allows us to solve for ice thickness. Here we assume that the ice deforms by creep and/or sliding when the basal shear stress is above a threshold value τ_y, consistent with Eq. (7), i.e.

$$h\sin S = \tau_\gamma \tag{10}$$

Expanding Eq. (10) in terms of the derivatives of z and h with respect to the cross-sectional direction x and along-slope direction y gives

$$h\sqrt{\frac{z_y^2 + (z_x + h_x)^2}{1 + z_y^2 + (z_x + h_x)^2}} = \tau_\gamma \tag{11}$$

where z_x is the derivative of z with respect to x, and z_y is the derivative of z with respect to y. Substituting Eqs. (9) and (10) into Eq. (11) gives

$$\frac{\tau_\gamma}{\sin\theta}\sqrt{\frac{\tan^2\theta + \left(\frac{2\pi\varepsilon}{\lambda}(1-h_1)\sin\left(\frac{2\pi x}{\lambda}\right)\right)^2}{1 + \tan^2\theta + \left(\frac{2\pi\varepsilon}{\lambda}(1-h_1)\sin\left(\frac{2\pi x}{\lambda}\right)\right)^2}} = \tau_\gamma \tag{12}$$

An approximate solution to Eq. (12) is

$$h_1 = \frac{\frac{\tau_\gamma}{\sin^2\theta\lambda}}{1 + \frac{\tau_\gamma}{\sin^2\theta\lambda}} \tag{13}$$

For $\lambda \ll \tau_\gamma/\sin^2\theta$, $h_1 \approx 1$, i.e. the ice surface is flat in the cross-sectional direction. In the opposite limit of large λ, $h_1 \approx 0$, i.e. the ice surface parallels the bed topography.

The goal of a linear stability analysis is to compute the growth rate of incipient valleys to first order in the amplitude ε. As such, terms of order ε^2 can be neglected from the analysis, keeping in mind that the results will only be applicable for small ε (i.e. the initial phase of valley deepening starting from initially-undissected topography). The first step of the analysis is to solve for the basal sliding velocity to first order in ε. Combining Eqs. (2), (5), (8), and (9) gives

$$u_s \approx c\tau_y^2\left(1 + 2\varepsilon e^{iX}\left(\rho g\sin\theta h_1 + \frac{\tau_y}{\tan\theta}\frac{2\pi}{\lambda}e^{i\frac{\pi}{2}}(1-h_1) - \mu c\tau_y^2\left(\frac{2\pi}{\lambda}\right)^2\right)\right) \tag{14}$$

In Eq. (14), the sinusoidal terms have been written using complex exponential notation. In this formulation, the cos term is replaced with $\exp(iX)$, where $X = 2\pi x/\lambda$. Substitution of Eq. (14) into Eq. (1) gives, to first order in ε:

$$\frac{\partial z}{\partial t} = -a|u_s|^b = -ac\tau_y^{2b} - abc\tau_y^2 u_{s1} = -E - \dot{\varepsilon}e^{iX} \tag{15}$$

where u_{s1} is the perturbation of u_s in Eq. (14), E is the average erosion rate and $\dot{\varepsilon}$ is the derivative of ε with respect to time. The solutions for the average erosion rate E and the dimensionless growth rate of the perturbations in bed topography, $\dot{\varepsilon}/\varepsilon$, are given by

$$E = ac\tau_y^b \tag{16}$$

and

$$\frac{\dot{\varepsilon}}{\varepsilon} = \frac{1}{2abc\tau_y^2}\left(\rho g\sin\theta h_1 - \mu c\tau_y^2\left(\frac{2\pi}{\lambda}\right)^2\right) \tag{17}$$

Eq. (17) is obtained by analyzing just the real part of complex Eq. (14). Only the real part is used because it is this part that is "in phase" with variations in bed topography and hence it is this and only this part that controls whether bed perturbations grow or decay over time. Eq. (17) quantifies how quickly sinusoidal variations in bed topography grow as a function of the model parameters and the wavelength of the bed (assuming the linear conditions appropriate early on in the valley-forming instability). The dimensionless growth rate $\dot{\varepsilon}/\varepsilon$ can take on both positive (growing perturbations) and negative values (decaying perturbations) depending on whether the ice thickening effect (the first term in Eq. (17)) is greater to or less than the viscous drag effect (the second term in Eq. (17)). Fig. 4 plots the dimensionless growth rate $\dot{\varepsilon}/\varepsilon$ as a function of λ for a reference case with $\tau_\gamma = 0.3$ bar, $\mu c = 0.001$ m Pa^{-1}, and $\sin\theta = 0.03$ on Earth ($g = 9.81$ m^2 s^{-1}), illustrating which wavelengths grow (i.e. $\dot{\varepsilon}/\varepsilon$ is greater than zero) versus which decay ($\dot{\varepsilon}/\varepsilon$ is less than zero). Fig. 4B,C, D illustrates the dependence of the instability on variations in that

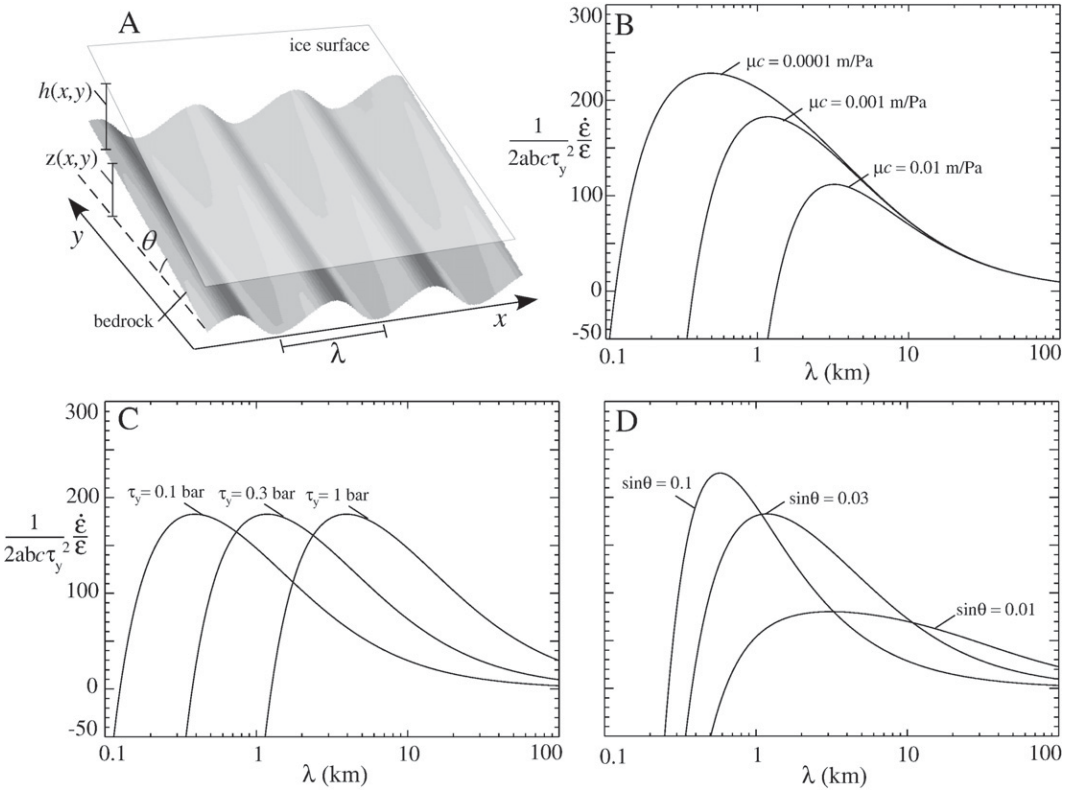

Fig. 4. Illustration and results of the linear stability analysis of Section 3.2. (A) Schematic diagram of the linear stability analysis, illustrating a sloping bedrock with sinusoidal cross-sectional bed variations. (B–D) Plots of the dimensionless growth rate of the bed perturbations as a function of the wavelength λ illustrating the model dependence on variations in (B) μc, (C) τ_y, and (D) $\sin\theta$.

values of μc, τ_y, and $\sin\theta$, respectively. Fig. 4B illustrates that, as the value of μc increases, the fastest-growing wavelength also increases, reflecting the fact that an increase in effective viscosity inhibits the formation of glacial valleys over a wider range of values at the low end of the wavelength spectrum. The dependence between the fastest-growing wavelength and μc is nonlinear, however, since an increase in μc by two orders of magnitude increases the fastest-growing wavelength by less than one order of magnitude. Increasing the value of the yield stress τ_y increases the value of the fastest-growing wavelength by approximately the same factor (Fig. 4C). Increasing the value of $\sin\theta$ (Fig. 4D) results in a decrease in the value of the fastest-growing wavelength by approximately the same factor. The shape of these growth curves indicate that, for a given set of parameter values, there is a value of λ that represents an optimal compromise between thickening of flow and viscous/sidewall drag in incipient valleys. This fastest-growing wavelength can be determined analytically by approximating h_1 as $1-(\sin^2\theta/\tau_\gamma)\lambda$ and substituting this expression into Eq. (17), differentiating with respect to λ, and setting the result equal to zero to yield

$$\lambda_{max} \approx \frac{2\tau_y}{\sin\theta}\sqrt[3]{\pi^2 \mu c / (\rho g)^2} \tag{18}$$

Eq. (18) is not an exact expression; it relies on an approximation to h_1 (Eq. (13), the full expression for h_1, leads to a growth curve whose maximum value cannot be determined analytically, only graphically or numerically). As an example, Eq. (18) predicts $\lambda_{max} = 2.1$ km for $\tau_y = 1.0$ bar, $\mu c = 0.01$ m Pa^{-1}, and $\sin\theta = 0.1$. Eq. (18) predicts that λ_{max} is proportional to τ_y, is inversely proportional to $\sin\theta$, and increases as the cube root of μc. Since the average ice thickness is proportional to $\tau_y/\sin\theta$, Eq. (18) also implies that λ_{max} is approximately proportional to the average ice thickness.

3.3. Numerical model results

Linear stability analyses are useful for identifying the combination of model parameters that control the length scale of a given geomorphic instability. Once valleys begin to form in earnest, however, the linear assumptions of the model break down and hence a 3D numerical model is necessary. To the extent that valley formation in the nonlinear, large-amplitude regime of the model involves the deepening of glacial valleys established during the initial, linear phase of valley formation, however, the predictions of the linear stability analysis can be expected to hold at least approximately for large-amplitude glacial valleys.

One key aspect neglected by the linear stability analysis is the stabilizing effects of glacial erosion once overdeepenings form beneath a glacier. Alley et al. (2003) proposed that supercooling of subglacial meltwater in sufficiently overdeepened bed conditions would result in a cessation of glacial erosion. In our model, we include this effect by prescribing zero erosion during any time step of the model if the bed slope is antithetical to and 50% greater than the ice surface slope above it, as suggested by Alley et al. (2003). This effect stabilizes overdeepenings in the model; without it, unrealistically deep cirque features can form in the model for certain model parameter values given sufficient time.

The numerical model of this paper combines the stabilizing effect of Alley et al. (2003) with the approximate solutions to Eqs. (1), (2), and (6) on a raster grid. Eqs. (1), (2), and (6) prescribe the basal shear stress, sliding velocity, and erosion rate for a given time step using the thickness of the ice and the ice surface slope above each pixel. A complete model also requires an expression for conservation of ice mass. The mass accumulation function $M(x,y)$, together with the divergence of ice flux, controls changes in ice thickness according to the conservation of mass equation:

$$\frac{\partial h}{\partial t} = -\nabla \cdot \boldsymbol{q} + M(x,y) \tag{19}$$

where $\boldsymbol{q} = hu$ and u is the depth-averaged ice velocity. The function $M(x,y)$ can take on any values, but it is usually assumed to be a function of elevation with positive values for elevations above the equilibrium line altitude (ELA), z_{ELA}, increasingly linearly with altitude, and negative values (ablation) for elevations below the ELA, i.e.,

$$\begin{aligned} M &= m_1(z(x,y) - z_{ELA}) \text{ if } z(x,y) > z_{ELA} \\ M &= m_2(z(x,y) - z_{ELA}) \text{ if } z(x,y) < z_{ELA} \end{aligned} \tag{20}$$

In this paper we use $m_1 = 0.01\ \mathrm{yr}^{-1}$ and $m_2 = 0.03\ \mathrm{yr}^{-1}$ as the default values in Eq. (20). If m_2 is greater than m_1, ablation will occur at higher rates for a given distance below the ELA compared to mass accumulation at the same distance above the ELA.

Given h and S at a pixel during a given time step, the basal shear stress is calculated by solving Eq. (6) to yield

$$\tau_b = \frac{\sqrt{1 + 4\rho g h \sin S \mu c \left|\frac{\partial^2 z}{\partial x^2}\right|} - 1}{2\mu c \left|\frac{\partial^2 z}{\partial x^2}\right|} \tag{21}$$

Substituting Eq. (21) into Eq. (2) gives

$$u_s = \frac{c}{\left(2\mu c \left|\frac{\partial^2 z}{\partial x^2}\right|\right)^2} \left(4\rho g h \sin S \mu c \left|\frac{\partial^2 z}{\partial x^2}\right| - 2\sqrt{1 + 4\rho g h \sin S \mu c \left|\frac{\partial^2 z}{\partial x^2}\right|} \right) \tag{22}$$

which can be approximated as

$$u_s \approx \frac{c(\rho g h \sin S)^2}{1 + \mu c (\rho g h \sin S) \left|\frac{\partial^2 z}{\partial x^2}\right|} \tag{23}$$

If we further assume that the basal shear stress is everywhere equal to a prescribed threshold value τ_y, as in the linear stability analysis, Eq. (23) can be further simplified to

$$u_s = \frac{c\tau_y^2}{1 + \mu c \tau_y \left|\frac{\partial^2 z}{\partial x^2}\right|} \tag{24}$$

Eq. (24) states that the effect of viscous drag is to reduce the basal sliding velocity by factor of $(1 + \mu c \tau_y |\partial^2 z / \partial x^2|)^{-1}$. This approach is equivalent to the manner in which Herman and Braun (2008) introduced viscous drag into their model (i.e. via a prescribed "constriction factor," equal to the coefficient in front of the curvature term in Eq. (24)). Our approach, however, provides a relationship between the constriction factor and the fundamental mechanical properties of glacial flow.

Eq. (19) is implemented in the model using a discrete, raster-based algorithm. During each time step, a thickness of ice equal to $M(x,y)\Delta t$ is added to each pixel (or removed, if $M(x,y)$ is negative) until the basal shear stress exceeds τ_y (or, in the ablation area, removed until no ice remains). Excess ice, i.e. ice from pixels where the flow of ice entering the pixel from up-ice together with local (i.e. $M(x,y)\Delta t$) contributions minus the amount of ice that can be added to the pixel before the critical basal shear stress is exceeded, is partitioned to all neighboring pixels downice. The proportion of the excess ice delivered to each pixel downice is weighted by the local ice surface slope in each direction, including diagonals. This approach is broadly similar to the "balance velocity" method of Budd and Warner (1996), which computes the depth-averaged ice velocity given the geometry of an ice body (h and S) and a mass accumulation function (M). In the balance-velocity method, however, the geometry of the ice body is considered static. In our model, steady state is not assumed because the geometry of the ice evolves in response to the flow pathways of excess ice. The excess ice flow at each pixel during a given time step is divided by ice thickness to yield a depth-averaged velocity. The basal sliding velocity is assumed to be proportional to that depth-averaged velocity. The basal sliding velocities calculated in this manner are then multiplied by $(1+\mu c\ \tau_y|\partial^2 z/\partial x^2|)^{-1}$ and then entered into Eq. (1) to calculate the local erosion rate for that time step. The depth of erosion that occurs during a given time step is also controlled by the coefficient a in Eq. (1). The results of the model can be reported more generally, however, by presenting results for a given maximum amount of erosion or thickness of rock removed from any one point in the grid. Depending on the value of a, 3 km of rock removal may require 3 or 30 Myr to accomplish, but the final landforms will be identical. As such, we report the model results for a prescribed value of the maximum amount of rock removal rather than as a function of time for specific values of a.

The model also includes isostatic rebound using a simplified algorithm. Isostatic rebound is calculated by computing the average erosion rate in the model domain during a given time step and then applying an uplift rate equal to 80% of that average erosion rate during the next time step. The 80% value comes from typical values for the relative density of crust and mantle rock. This approximate method is adequate for this application because glacial valleys form in the model at a spatial scale much lower than the flexural wavelength of the lithosphere. As such, it is not essential for the model to reproduce the details of the flexural solution for this particular application. On Mars, isostatic rebound at scales of tens to hundreds of kilometers is not significant due to the relatively large elastic thickness. As such, we do not include isostatic rebound in the application of the model to Mars. Including isostatic rebound in the terrestrial model application is not essential for creating periodic glacial valleys, but it does ensure that "mature" glacial valleys form in the model. Without isostatic rebound, glacial erosion slows down and eventually ceases as topography that began above the ELA is denuded below the ELA.

Fig. 5 illustrates the results of the model for an initially-undissected, plateau-dominated landscape (initial topography shown in Fig. 5A) that is 20 km by 60 km with a maximum elevation of 2 km, and $\tau_y = 0.4$ bar, $z_{ELA} = 0.8$ km, $b = 1$, and $\mu c = 1.0\ \mathrm{m\ Pa}^{-1}$, $m_1 = 0.01$ and $m_2 = 0.03$. Fig. 5B,C illustrates the topography of the model after 3 km of rock removal by glacial erosion has taken place. Bowl-shaped cirques form on the plateau with a characteristic spacing of approximately 3 km in this example. Cirques feed into glacial valleys and outlet glaciers with a similar spacing as the cirque basins on the plateau. It should be emphasized that the periodic valleys created by the model are entirely a self-organized feature of the model — the initial topography has no initial grooves at any scale. The relative values of m_1 and m_2 control how far glacial erosion takes place downslope from the equilibrium line. If $m_1 = m_2$, outlet glaciers will extend, tongue-like, farther out into the basin surrounding the range than they do in this model. We choose a relatively large value for m_2/m_1 (i.e. the ablation rate increases rapidly with vertical distance below the ELA) in order to limit the size of the model domain needed to fully encompass the outlet glaciers. It should be noted that the value for μc assumed in this example is somewhat larger than the range of values of this parameter combination estimated for terrestrial glaciers. However, the choice of this value for μc yields values for valley spacing comparable to those on Earth. The relatively high value of μc offsets the fact that bed slopes are quite steep in this example (i.e. a drop of 2000 m at the plateau edge over a distance of several kilometers).

Fig. 6 illustrates the effect of varying the value of τ_y from 0.2 to 0.8 bars and the value of μc from 0.01 to 1.0 m Pa^{-1} in the model. In each case, the final bed topography is shown once a maximum of 3 km of rock removal by glacial erosion has occurred. Cirque valleys increase in spacing in direct proportion to the value of τ_y mean spacings are 1.5 km for $\tau_y = 0.2$ bars (Fig. 6A), 2.8 km for $\tau_y = 0.4$ bars (Fig. 6B), and 5.5 km for $\tau_y = 0.8$ bars, (Fig. 6C) assuming $\mu c = 1.0\ \mathrm{m\ Pa}^{-1}$. Valleys increase in spacing more slowly with increasing values of μc: mean spacings are 0.7 km for $\mu c = 0.01\ \mathrm{m\ Pa}^{-1}$ (Fig. 6D), 1.3 km for $\mu c = 0.1\ \mathrm{m\ Pa}^{-1}$ (Fig. 6E), and 2.8 km for $\mu c = 1.0\ \mathrm{m\ Pa}^{-1}$ (Fig. 6B)

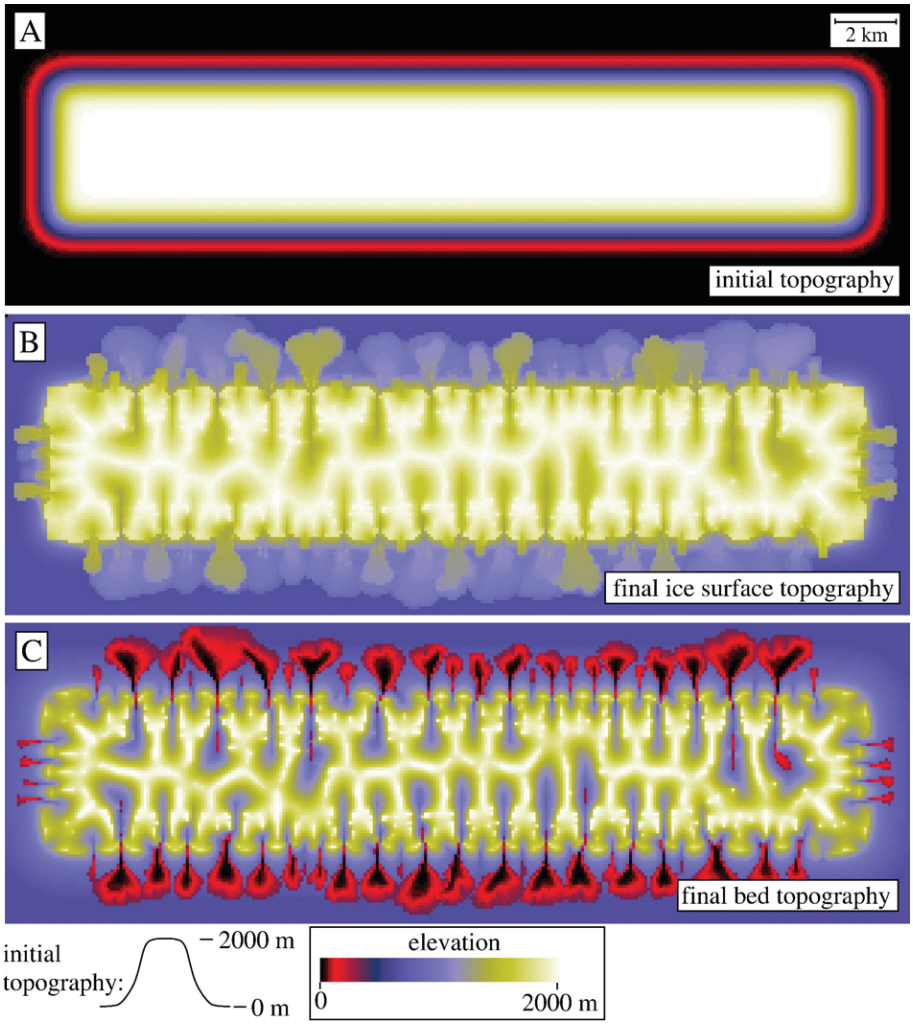

Fig. 5. Maps of the input and output topography of the numerical model. (A) The initial 20×60 km plateau-dominated landscape of the model, (B) the final ice surface topography predicted by the model for the reference case with an equilibrium line altitude (ELA) of 0.8 km, $\tau_y = 0.4$ bars, and $\mu c = 1.0$ m Pa^{-1}, and (C) the final bed topography for the same model.

assuming $\tau_y = 0.4$ bars. It is difficult to compare the results of the 3D model precisely with the linear stability analysis of Section 3.2 because the bed slope is not constant in this plateau-dominated landscape, but instead varies from flat to steeply-sloping as one moves from plateau interior to plateau margin. Nevertheless, Fig. 7 illustrates good agreement between the trends predicted by the linear stability analysis and the results of the 3D model for a range of parameter values. Fig. 7 plots the results of 21 model simulations with the plateau-dominated initial condition of Fig. 6 with three different values of τ_y and seven different values of μc. The straight lines indicate the predicted trends of the linear stability analysis (i.e. spacing is proportional to τ_y and proportional to the cubed root of μc), showing good agreement with the results of the 3D model. Model results (not shown) were also obtained by varying the exponent b from 1 to 3 in Eq. (1) keeping all other parameters constant. The spacing of glacial valleys did not vary as a function of b, a result consistent with the predictions of the linear stability analysis.

Initially-undissected topography is an appropriate starting point for investigating the self organization of glacial valleys. On Earth, however, most if not all glacial valleys are influenced to some degree by the presence of preexisting fluvial valleys. Fluvial valleys can also be periodic, so it is reasonable to ask whether some periodic glacial valleys may be relict features inherited from earlier periods of predominantly fluvial erosion. To determine the effect of preexisting fluvial valleys on the spacing of glacial valleys, we performed a two-phase model experiment in which an initially-fluvially-dominated landscape was subjected to glaciation at time zero (Fig. 8). The initial topography in Fig. 8A was created using a stream-power bedrock channel erosion model (Whipple and Tucker, 1999) in which the erosion rate is a function of drainage area, A_d, and along-channel slope, $\partial z/\partial x$:

$$\frac{\partial z}{\partial t} = U - KA_d^{1/2}\left|\frac{\partial z}{\partial x}\right| \tag{25}$$

where U is the rock uplift rate and K is the bedrock erodibility coefficient. This model was run forward in time until an approximate steady-state topographic condition was achieved. The values of U and K were chosen to yield a maximum elevation of 2 km in steady state so that the total relief of this fluvial landscape would be comparable to the plateau-dominated initial condition of Fig. 6. Outlet channels in the fluvial topography (Fig. 8A) have a characteristic spacing, a result that is commonly observed in drainage basin evolution models in which a significant regional slope exists (e.g. Perron et al., 2008). The location of large outlet fluvial valleys sets the location of the resulting outlet glacial valleys, but glacial erosion widens smaller V-shaped valleys into wide U-shaped valleys with a larger characteristic spacing (Fig. 8B). Glacial erosion acts to filter out the small, narrowly-spaced low-order fluvial valleys above the ELA because viscous drag in these

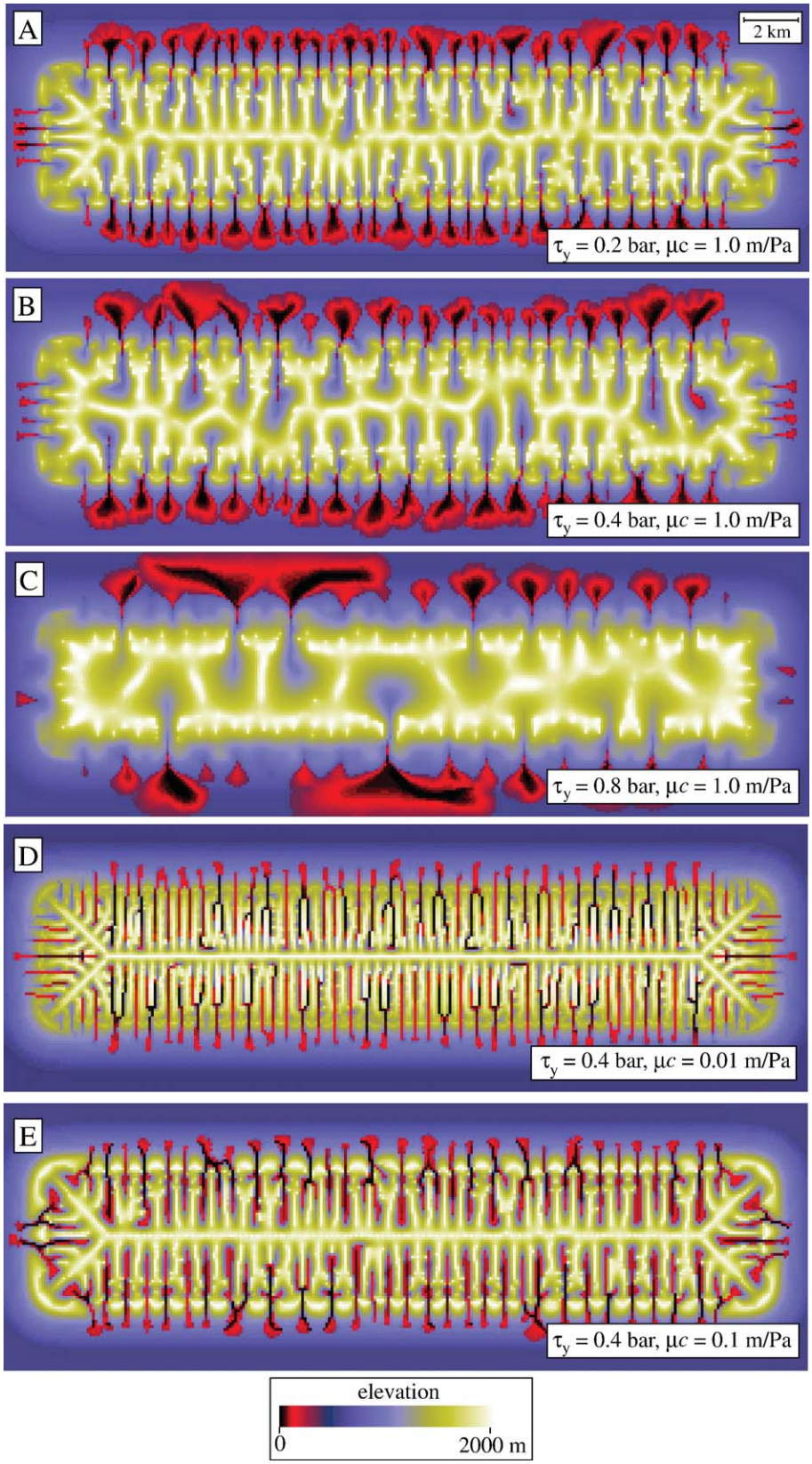

Fig. 6. Maps of the final bed topography predicted by the numerical model with an initial plateau-dominated landscape, illustrating the dependence of the model on the parameters τ_y and μc for a constant ELA of 0.8 km. Results for (A) $\tau_y = 0.2$ bars, $\mu c = 1.0$ m Pa^{-1}, (B) $\tau_y = 0.4$ bars, $\mu c = 1.0$ m Pa^{-1}, (C) $\tau_y = 0.8$ bars, $\mu c = 1.0$ m Pa^{-1}, (D) $\tau_y = 0.4$ bars, $\mu c = 0.01$ m Pa^{-1}, and (E) $\tau_y = 0.4$ bars, $\mu c = 0.1$ m Pa^{-1}.

valleys limits the ability of the ice to incise into such narrow valleys. As a result, valleys with spacings smaller than λ_{max} are replaced with valleys spaced by values closer to λ_{max}. This "resetting" of the landscape by glacial erosion takes time to occur in the model and in nature. Based on the results of this model, as a rule of thumb the amount of maximum rock removal in the model must exceed twice

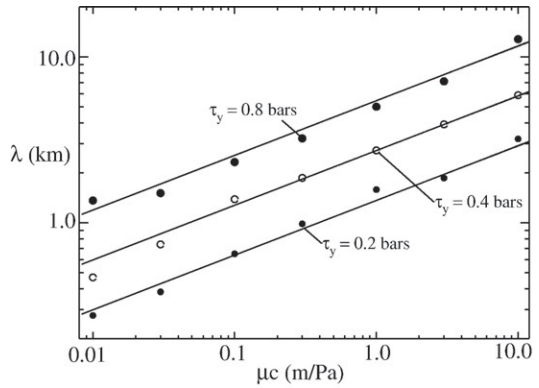

Fig. 7. Plots of glacial valley spacing measured from output of the numerical model with a plateau-dominated initial condition (see Figs. 5 and 6) for a range of values of τ_y and μc. Note logarithmic scales on both axes. Straight lines correspond to the power-law relationship between spacing and μc predicted by the linear stability analysis.

the initial relief of the landscape (i.e. 4 km of maximum rock removal compared to 2 km of initial relief) in order for glacial processes to be fully imprinted on the landscape.

The plateau-dominated and fluvially-incised initial conditions of Figs. 6 and 8 are appropriate for terrestrial glaciers but not for Mars. The topography of Mars is dominated by impact craters that have been modified over time by mass wasting. In order to provide the model with an initial landscape representative of the mid-latitude regions of Mars, we obtained a synthetic landscape subjected to meteor impacts and mass wasting from Shane Byrne of the University of Arizona (Shane Byrne, personal communication, 2009). This synthetic landscape was produced using a numerical model similar to that of Richardson et al. (2004). The model generates impact craters with a frequency-size distribution comparable to that of actual craters and degrades them over time using a slope-dependent transport model for regolith coupled with conservation of mass. Example output from this model is shown in Fig. 9A prior to the introduction of glaciers. Note the significantly larger spatial scale of this model domain (e.g. 128 × 128 km) compared to that of the terrestrial model example of Fig. 6. For this model experiment, the entire surface was assumed to be covered in ice (i.e. the ELA was set to zero) and a uniform mass accumulation rate was prescribed. The value of g was set for Mars (i.e. $g = 3.72\ \mathrm{m\ s^{-2}}$) and the threshold basal shear stress was assumed to be 0.4 bars, consistent with the calibration of Banks and Pelletier (2008). It should be emphasized that the calibration of threshold basal shear stress of Banks and Pelletier (2008) corresponds to modern conditions that may not be applicable to other time periods on Mars. Nevertheless, using the observed ice thicknesses on Mars today provides the best available calibration for the threshold basal shear stress parameter.

The output of the model after a maximum of 3 km of rock removal has occurred is shown in Figs. 9B–C for $\tau_y = 0.4$ bars and $\mu c = 1.0$ and $10.0\ \mathrm{m\ Pa^{-1}}$, respectively. We choose larger values for μc in this example because colder ice on Mars leads to higher viscosity values. We will discuss this point in detail in Section 4 below. As in Fig. 6, glacial valley formation selects a preferred wavelength or spacing that is related to the values of τ_y and μc. Mean spacings are harder to quantify precisely in this case due to the more complex (i.e. cratered) nature of the pre-glacial landscape, but estimates for glacial valley spacing predicted by the model are approximately 10–30 km for the two values of μc chosen (with increasing spacing for the higher value of μc). This range of values is consistent with characteristic spacing of cirque-like basins of the Argyre and Hellas regions of Mars, which also range from approximately 10 to 30 km.

4. Discussion and conclusions

The model results in this paper provide a preliminary basis for understanding the controls on the spacing of low-order glacial valleys on Earth and Mars. The results suggest that valley slope, the threshold basal shear stress for ice motion, effective ice viscosity, bed friction, and gravity all control the spacing of low-order glacial valleys. Based on the characteristic scales of glacial valley spacing on Earth (1–3 km) and Mars (10–30 km) and the model prediction $\lambda_{max} = 2(\tau_y / \sin\theta)\sqrt[3]{\pi^2 \mu c / (\rho g)^2}$, the inferred values of the product of μc is in the range of

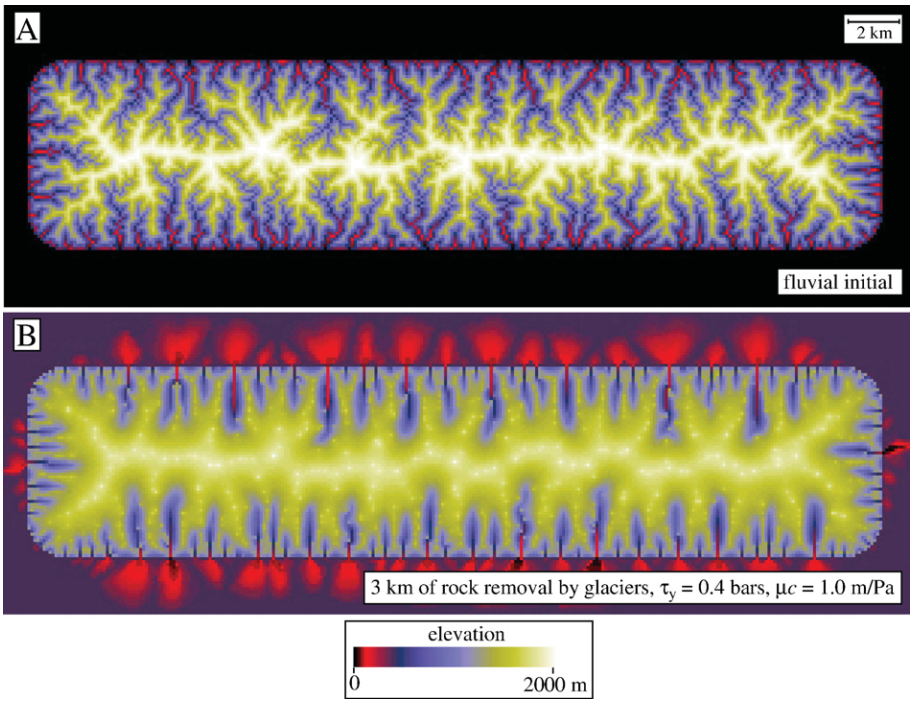

Fig. 8. Illustration of the model results with initially-fluvially-dissected topography. (A) Initial topography input to the model, produced by running a stream-power model of bedrock channel erosion by fluvial processes to an approximate topographic steady-state condition. (B) Map of the final bed topography predicted by the numerical model with $\tau_y = 0.4$ bars and $\mu c = 1.0\ \mathrm{m\ Pa^{-1}}$ after 3 km of maximum erosion has occurred.

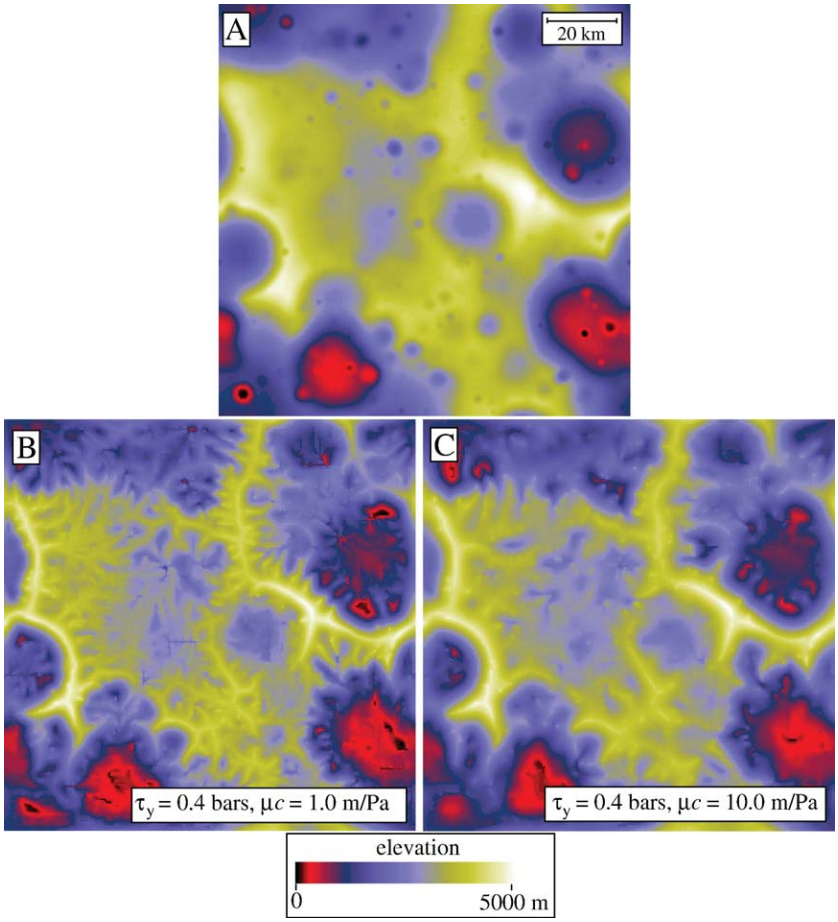

Fig. 9. Maps of the final bed topography predicted by the numerical model with an initially-cratered domain 128×128 km, illustrating the dependence of the model on the fundamental parameters. (A) Initial topography. Results for $\tau_y = 0.4$ bar and (B) $\mu c = 1.0$ m Pa^{-1}, (C) $\mu c = 10.0$ m Pa^{-1}.

0.01–0.1 m Pa^{-1} for terrestrial paleoglaciers in the western United States, assuming a typical bed slope of 0.1 and a yield stress of 0.3 bars. Given that bed slopes/relief ratios are 2–6 times lower on Mars, the model predicts that glacial valley spacing on Mars will be approximately 2–6 times greater than on Earth, all else being equal. As such, lower bed slopes can partly account for why glacial valley spacing on Mars is more than an order of magnitude greater than on Earth. Since ice viscosity is strongly controlled by temperature, the model also suggests that differences in ice temperature between the two planets may also account for part of the difference in the characteristic scales of glacial valley formation.

Fig. 10 plots the relationship between the rate coefficient in Glen's flow law (1952), A, and ice temperature T. For a given basal shear stress, the values of μ and A are inversely proportional, so the data plotted in Fig. 10 provides a basis for relating μ to the mean ice temperature T. Solid circles in Fig. 10 are the values for A recommended by Paterson (2000) based on measured data for terrestrial glaciers (higher temperatures) and a model based on thermally-activated creep (lower temperatures). The temperature of glacial ice varies as function of depth below the surface of the glacier. As a result, viscosity will also vary with depth. Temperatures at the base of a glacier are controlled by the mean annual temperature at the surface, the geothermal gradient, the friction produced by sliding along the bed, and the heat released or absorbed by freezing or melting, respectively. The vertically-averaged ice temperature in a warm-based glacier can be roughly approximated, however, as the average of 0 °C (i.e. the temperature near the bed) and the mean annual surface temperature. Ice a few meters below the glacier surface will be equilibrated to the mean annual surface temperature while ice near the base of the glacier must be close to 0 °C (assuming a warm-based glacier). Colder bed conditions are possible, of course, but do limited geomorphic work if the temperature of the ice is significantly below 0 °C because the ice will be frozen to its bed and no sliding will occur. The modern mean annual surface temperatures of terrestrial glaciers are in the range of −20 to 0 °C. Higher temperatures do occur in outlet glaciers that extend far out into the ablation zone, but those cases are not relevant to the low-order glacial valleys considered here.

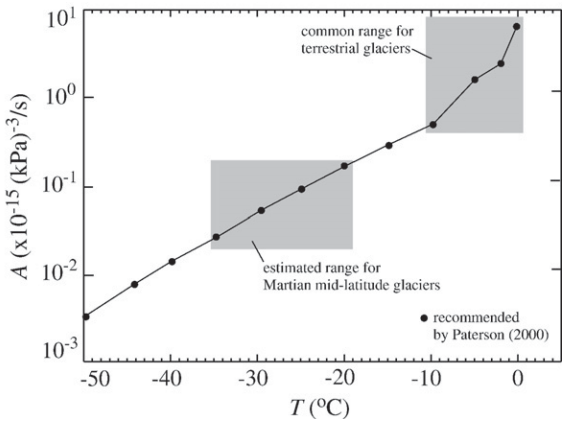

Fig. 10. Plot of the relationship between the coefficient in Glen's flow law (1952), A, and ice temperature T. Solid circles are values recommended by Paterson (2000) based on measured data for terrestrial glaciers (higher temperatures) and models for thermally-activated creep of ice (lower temperatures). Common ranges for terrestrial glaciers and estimated range for Martian mid-latitude glaciers also shown.

In the Martian midlatitudes from 45° to 60°, mean annual modern surface temperatures are in the range of −70 to −40 °C based on the methods of Leighton and Murray (1966). Using these temperature ranges, we can approximate the depth-averaged temperatures of glacial ice on Earth and Mars to be within a range from −10 to 0 °C and −35 to −20 °C, respectively (Fig. 10). Of course, temperatures on both Earth and Mars are a function of climate (glacial/interglacial cycles on Earth and variations in orbital obliquity on Mars). As such, any estimate based on modern temperatures is only a rough approximation. Nevertheless, based on the data illustrated in Fig. 10 and the assumption that relative temperatures between Earth and Mars today are broadly applicable to past epochs, it is possible to estimate that the value of μc for Martian midlatitudes is approximately 30–50 times higher than the value for terrestrial paleoglaciers, i.e. in the range of 0.3–5.0 m Pa^{-1} if we assume μc is in the range of 0.01–0.1 m Pa^{-1} on Earth and that the value of the bed friction c remains the same. Values within this range were chosen for the initially-cratered experiments illustrated in Fig. 9. Those experiments predict characteristic glacial valley spacings in the range of 10–30 km, i.e. within the range of spacings observed on Mars. It should be emphasized that the larger value of valley spacings on Mars cannot be uniquely interpreted in terms of differences in bed slope and temperature-dependent viscosity. Gravity does play a role in controlling spacing, as indicated in Eq. (18), but this effect is likely to be partially offset by lower threshold basal shear stresses on Mars, as documented by Banks and Pelletier (2008) based on a comparison of the yield stresses inferred from the geometries of modern ice caps on Earth and Mars. Nevertheless, the hypothesis that differences in bed slope and ice viscosity play the dominant roles in controlling the difference in characteristic scales of glacial erosion is consistent with the model results and independent constraints available on model parameters.

In this paper we developed analytic and numerical solutions of a coupled numerical model for alpine glacial flow and subglacial bedrock erosion to quantitatively determine the controls on the spacing of low-order glacial valleys. The characteristic spacing of glacial valleys produced by the model is controlled by a competition between the thickening of ice flow into incipient glacial valleys, which acts to enhance flow and valley deepening, and viscous drag, which acts to limit flow and deepening. The glacial valley spacing that represents the best compromise between these two competing effects is found to be a function of valley slope, the threshold basal shear stress for ice motion, the effective ice viscosity, a bed-friction parameter, and gravity. The model predicts that glacial valleys on Mars are larger than those on Earth, based primarily on differences in valley slope and temperature-dependent ice viscosity between the two planets.

Acknowledgements

This study was funded by the Mars Data Analysis Program grant #NNX07AR41G. Thanks to Shane Byrne for graciously sharing his synthetic cratered landscape. We wish to thank Goro Komatsu and Jan Kalvoda for reviews that improved the manuscript, and Takashi Oguchi for his careful editing of the text.

References

Alley, R.B., Lawson, D.E., Larsen, G.J., Evenson, E.B., Baker, G.S., 2003. Stabilizing feedbacks in glacier-bed erosion. Nature 424, 758–760.
Banks, M., Pelletier, J.D., 2008. Numerical modeling of ice-cap geometry over cratered terrain: application to the south polar region of Mars. Journal of Geophysical Research 113. doi:10.1029/2007JE002895.
Banks, M.E., McEwen, A.S., Kargel, J.S., Baker, V.R., Strom, R.G., Mellon, M.T., Gulick, V.C., Keszthelyi, L., Herkenhoff, K.E., Pelletier, J.D., Jaeger, W.L., 2009. HiRISE observations of glacial and periglacial morphologies in the Circum-Argyre Planitia Highlands, Mars. Journal of Geophysical Research 113, E12015. doi:10.1029/2007JE002994.
Boulton, G.S., 1974. Processes and pattern of glacial erosion. In: Coates, D.R. (Ed.), Glacial Geomorphology. Proc. Binghamton Geomorphology Symp., State Univ. N.Y., Binghamton, pp. 41–87.
Budd, W.F., Warner, R.C., 1996. A computer scheme for rapid calculations of balance-flux distributions. Annals of Glaciology 23, 21–27.
Clark, B.R., Mullin, R.P., 1976. Martian glaciation and the flow of solid CO_2. Icarus 27, 215–228.
Glen, J.W., 1952. Experiments on the deformation of ice. Journal of Glaciology 2, 111–114.
Hallet, B., 1979. A theoretical model of glacial abrasion. Journal of Glaciology 23, 39–50.
Hallet, B., Hunter, L., Bogen, J., 1996. Rates of erosion and sediment evacuation by glaciers: a review of field data and their implications. Global and Planetary Change 12, 213–235.
Harbor, J.M., 1992a. Application of a general sliding law to simulating flow in a glacier cross section. Journal of Glaciology 38, 182–190.
Harbor, J.M., 1992b. Numerical modeling of the development of U-shaped valleys by glacial erosion. Geological Society of America Bulletin 104, 1364–1375.
Harbor, J.M., 1992c. On the mathematical description of glaciated valley cross sections. Earth Surface Processes and Landforms 17, 477–485.
Herman, F., Braun, J., 2008. Evolution of the glacial landscape of the southern Alps of New Zealand: insights from a glacial erosion model. Journal of Geophysical Research 113. doi:10.1029/2007JF000807.
Holt, J.W., Safaeinili, A., Plaut, J.J., Head, J.W., Phillips, R.J., Seu, R., Kempf, S.D., Choudary, P., Young, D.S., Putzig, N.E., Biccari, D., Gim, Y., 2008. Radar sounding evidence for buried glaciers in the southern mid-latitudes of Mars. Science 322, 1235–1238.
Kargel, J.S., 2004. Mars: A Warmer Wetter Planet. Springer-Verlag, New York. 557 pp.
Kargel, J.S., Strom, R.S., 1992. Ancient glaciation on Mars. Geology 20, 3–7.
Leighton, R.B., Murray, B.C., 1966. Behavior of carbon dioxide and other volatiles on Mars. Science 153, 136–144.
MacGregor, K.C., Anderson, R.S., Anderson, S.P., Waddington, E.D., 2000. Numerical modeling of glacial erosion and headwall processes. Geology 28, 1031–1034.
MacGregor, K.C., Anderson, R.S., Waddington, E.D., 2009. Numerical simulations of glacial-valley longitudinal profile evolution. Geomorphology 103, 189–204.
Nye, J.F., 1951. The flow of glaciers and ice-sheets as a problem in plasticity. Proceedings of the Royal Society of London, Series A 229, 554–572.
Paterson, W.S.B., 2000. The Physics of Glaciers, Third edition. Pergamon Press, Oxford. 481 pp.
Perron, J.T., Dietrich, W.E., Kirchner, J.W., 2008. Controls on the spacing of first-order valleys. Journal of Geophysical Research 113, F04016. doi:10.1029/2007JF000977.
Plaut, J.J., Safaeinili, A., Holt, J.W., Phillips, R.J., Head III, J.W., Seu, R., Putzig, N.E., Frigeri, A., 2009. Radar evidence for ice in lobate debris aprons in the mid-northern latitudes of Mars. Geophysical Research Letters 36, L02203. doi:10.1029/2008GL036379.
Richardson, J.E., Melosh, H.J., Greenberg, R.J., 2004. Impact-induced seismic shaking on asteroid 433 Eros: a surface modification process. Science 306, 1526–1529.
Seddik, H., Sugiyama, S., Naruse, R., 2005. Numerical simulation of glacial-valley cross-section evolution. Bulletin of Glaciological Research 22, 75–79.
Smith, D., Neumann, G., Arvidson, R.E., Guinness, E.A., Slavney, S., 2003. Mars Global Surveyor Laser Altimeter Mission Experiment Gridded Data Record. NASA Planetary Data System, MGS-M-MOLA-5-MEGDR-L3-V1.0.
Tomkin, J.H., Braun, J., 2002. The effect glaciation has on the relief of a fast growing orogen: a numerical modelling study. American Journal of Science 302, 169–190.
Weertman, J., 1957. On the sliding of glaciers. Journal of Glaciology 3, 33–38.
Whipple, K.X., Tucker, G.E., 1999. Dynamics of the stream power river incision model: implications for height limits of mountain ranges, landscape response timescales and research needs. Journal of Geophysical Research 104, 17,661–17,674.